Damping in Free Layers of Spin-Transfer-Torque Magnetic Memory at Elevated Temperatures

Adam Whitney[1], Chuanpu Liu,[1] Tiffany S. Santos[2], Rajesh V. Chopdekar[2], Matthew Carey,[2] Galen Street,[1] Vijaysankar Kalappattil,[1] Keira Leistikow,[1] and Mingzhong Wu[1,*]

[1] *Department of Physics, Colorado State University, Fort Collins, Colorado 80523, USA*

[2] *Western Digital Research Center, Western Digital Corporation, San Jose, California 95119, USA*

In spin-transfer-torque (STT) magnetic random-access memory (MRAM), both switching current and switching time depend on the damping of the free layer. It is known that the magnetic damping constant (α) varies with temperature; because STT MRAM cells operate well above room temperature, there is an urgent need to determine and understand damping properties in STT MRAM free layers at elevated temperatures. This paper reports on comparative studies of high-temperature frequency-dependent ferromagnetic resonance (FMR) in two STT MRAM free layers: (i) a low-α free layer with split W layers, and (ii) a conventional free layer with a single W layer. Comprehensive FMR measurements and analyses show that (1) the damping constant of the low-α free layer is always smaller than that in the conventional free layer, as the temperature increases from 300 to 520 K; (2) the damping constant increases monotonically with temperature in both the free layers; and (3) the damping increase is relatively modest in the low-α free layer, from about 0.0035 to about 0.0079, but is more pronounced in the conventional free layer, from about 0.0092 to about 0.028. These results can be interpreted in terms of the temperature dependence of the damping produced by spin-flip magnon-electron scattering and the difference of the Curie temperatures in the two free layers. They clearly establish the technological advantage of the low-α free layer over the conventional free layer from the perspective of the STT MRAM application. In addition, the high-temperature FMR data also yield important information about the temperature dependence of the effective perpendicular anisotropy field and the origin of the inhomogeneous line broadening in the free layers.

I. INTRODUCTION

A spin-transfer-torque (STT) magnetic random-access memory (MRAM) cell is usually composed of three layers: (1) a free layer, the magnetization of which can be switched by STT between two distinct directions, corresponding to binary values; (2) a reference layer that has fixed magnetization and works as a spin polarizer to produce spin currents for the free layer; and (3) a nonmagnetic barrier, such as an MgO layer, that physically separates the free and reference layers [1,2]. Ideal STT MRAM devices require that (1) the critical current density, J_c, needed to switch the free layer is minimized, and (2) an effective thermal stability parameter, Δ, is maximized. In general, J_c is proportional to the product of the thickness, t_F; saturation magnetization, M_s; and Gilbert damping constant, α, of the free layer, namely, $J_c \propto t_F M_s \alpha$, and Δ scales with M_s and the perpendicular anisotropy field, H_u, and is inversely proportional to temperature T, namely, $\Delta \propto H_u M_s / T$ [3,4]. One can see that a desired

free layer should be thin and have low damping, while exhibiting large magnetization and strong anisotropy at the same time.

The STT MRAM free layer is often made of a Co-Fe-B/W/Co-Fe-B trilayered structure, where W can be replaced by other metals, such as Ta or Mo. The roles of the W layer in this "conventional" free layer are (1) to absorb boron during annealing and thereby ensure solid-phase epitaxy at the Co-Fe-B/MgO interface, and (2) to help realize strong perpendicular anisotropy in the Co-Fe-B layers [5,6]. However, the W layer unfortunately creates dead layers, which reduce the effective M_s and enhance the damping of the free layer, resulting in a higher J_c. The use of two ultrathin W layers is shown to be a way to improve free-layer properties compared to a single W layer [7,8]. Santos *et al.* recently proposed to split the single W layer into two thinner layers, and thereby, mitigate W-produced damping enhancement and dead layers [8]. Specifically, they fabricated a Co-Fe-B/Co-Fe/Mg/W/Co-Fe/Mg/W/Co-Fe structure with two ultrathin W layers that showed a reduced α, a reduced t_F, and an increased M_s when compared with the

---

*mwu@colostate.edu; min.wu@northeastern.edu

conventional free layer with a single W layer. The STT MRAM device built on this low-α free layer showed a lower J_c and a higher Δ than the device made of the conventional free layer [8].

This paper reports on comparative studies of high-temperature frequency-dependent ferromagnetic resonance (FMR) in (1) the low-α free layer with split W layers, and (2) the conventional free layer with a single W layer, which are described above. Comprehensive FMR measurements show that, over the temperature (T) range from 300 to 520 K, the damping constant of the low-α free layer is always smaller than that of the conventional free layer. Furthermore, the damping constants in the two samples both increase monotonically with an increase in T, but at very different paces. Specifically, as T varies from 300 to 520 K, the damping constant in the low-α free layer increases nearly linearly, from about 0.0035 to about 0.0079, while the damping constant in the conventional free layer increases nearly exponentially, from about 0.0092 to about 0.028. These results can be interpreted in terms of the T dependence of the damping produced by spin-flip magnon-electron scattering [9–12] and the difference of the Curie temperatures in the two free layers [8]. They clearly establish the advantages of the low-α free layer over the conventional free layer from the perspective of the STT MRAM application.

It should be highlighted that the high-temperature damping properties reported below are of great technological significance because STT MRAM cells usually operate above room temperature. The temperature dependences and the differences between the low-α and conventional free layers have important implications for the future design and optimization of STT MRAM free layers. The high-T damping values presented below can also be used as firsthand input damping parameters for industrial modeling and simulations of STT MRAM devices.

II. SAMPLES AND MEASUREMENT TECHNIQUES

A. Free-layer samples

Two free-layer samples were measured and compared. The low-α free-layer sample, denoted as sample A in the following, is a multilayer of Co-Fe-B(0.6)/Co-Fe(0.1)/Mg(0.4)/W(0.02)/Co-Fe(0.32)/Mg(0.4)/W(0.02)/Co-Fe(0.32), where the numbers indicate layer thicknesses in nm. The total thickness of sample A is $t_F = 1.38$ nm. The conventional free-layer sample, denoted as sample B in the following, is a multilayer of Co-Fe-B(1.3)/Mg(0.6)/W(0.3)/Co-Fe-B(0.7), with a total thickness of $t_F = 2.3$ nm. Note that sample A has two W layers, while sample B has a single W layer. The Mg layers in the samples act as sacrificial layers to protect the Co-Fe-B layers during W deposition, and therefore, are not included in the total film thicknesses [8,13]. These free-layer samples were fabricated by sputtering in the following sequence on Si/SiO$_2$ substrates: nonmagnetic seed layer/MgO/free layer/MgO/Ru/Ta/Ru. A nonmagnetic seed layer was used instead of a magnetic reference layer to ensure that the only magnetic signal in our detailed magnetic characterization came from the free layer. All details about the fabrication and structural properties of these two samples are provided in Ref. [8]. The major magnetic properties of the samples are summarized in Table I. The table includes key results from this work, which are discussed in detail in Sec. III.

Three points should be made about the two samples. First, it is intentional to design sample A and sample B to have large differences in both the W thicknesses and the total free-layer thicknesses, which produce significant differences in M_s, the Curie temperature (T_c), and α. This ensures that the temperature dependences of the properties for the two samples are very different, thus making

TABLE I. Properties of MRAM free-layer samples: sample A and sample B. Thicknesses were determined according to the sputtering time and the deposition rate. The Curie temperature and saturation magnetization were measured with a physical property measurement system. All other parameters were determined through ferromagnetic resonance measurements.

Property	Sample A	Sample B
Structure	Co-Fe-B/Co-Fe/W/Co-Fe/W/Co-Fe	Co-Fe-B/Co-Fe/W/Co-Fe
Thickness, t_F (nm)	1.38	2.30
Curie temperature, T_C (K)	~900	~650
Saturation magnetization, M_s (emu/cm^3) (300 K)	1680	1033
Interfacial anisotropy constant, K_i (erg/cm^2) (300 K)	2.69	1.90
Effective anisotropy field, H_{eff} (kOe) (300 K)	2.15 ± 0.12	3.04 ± 0.04
Effective anisotropy field, H_{eff} (kOe) (520 K)	0.22 ± 0.07	0.39 ± 0.35
Damping constant, α (300 K)	$(3.5 \pm 0.9) \times 10^{-3}$	$(9.2 \pm 1.1) \times 10^{-3}$
Damping constant, α (520 K)	$(7.9 \pm 1.2) \times 10^{-3}$	$(28.0 \pm 5.8) \times 10^{-3}$
Inhomogeneous line broadening, ΔH_0 (Oe) (300 K)	133.1 ± 8.7	111 ± 11
Inhomogeneous line broadening, ΔH_0 (Oe) (520 K)	37.8 ± 12.1	18.9 ± 46.6

a more interesting comparison for this study of damping as a function of T. Second, the thicknesses of all the layers were determined according to the sputtering time and the film deposition rate. Third, given that the diameter of a tungsten atom is about 0.3 nm, sample B has just a single monolayer of W atoms, while sample A has a discontinuous monolayer of W atoms. As such, the W layers do not have enough atoms to establish a crystal structure. Thicker W layers deposited on Co-Fe-B layers have a β phase for thicknesses no larger than about 3.0 nm but have an α phase for thicknesses larger than about 3.0 nm.

B. Static magnetic properties

Magnetic hysteresis loops were measured on samples A and B over a temperature (T) range from room temperature (300 K) to 600 K. The measurements were carried out with a physical property measurement system (PPMS) under an in-plane magnetic field. Error function fits to those hysteresis loops yielded the saturation magnetization, M_s, and effective anisotropy field, $H_{\text{eff}} = H_u - 4\pi M_s$, of the two samples, where H_u is the perpendicular anisotropy field. Figure 1(a) presents the M_s against T data. One can see that, as T increases from 300 K to about 600 K, M_s decreases from about 1680 emu/cm^3 to about 1300 emu/cm^3 in sample A and from about 1030 emu/cm^3 to about 500 emu/cm^3 in sample B. These results suggest that sample A will have greater thermal stability than sample B, particularly at high temperature. Figure 1(b) gives the H_{eff} against T data. The data show that H_{eff} decreases monotonically in both samples and approaches zero near 575 K; H_{eff} in sample A is smaller than that in sample B, but the difference becomes smaller with an increase in T. The H_{eff} values are positive for the entire T range in both samples. This implies that the perpendicular anisotropy field, H_u, is higher than the demagnetization field, $4\pi M_s$, in both samples, which is a requirement for perpendicular

MRAM applications. The decrease of H_{eff} with temperature indicates that H_u decreases more than $4\pi M_s$ as T increases.

The $M_s(T)$ data in Fig. 1(a) also allow for the evaluation of the Curie temperatures (T_C) of the samples. Specifically, if one fits the $M_s(T)$ response to the Kuz'min equation [14–16],

$$M_s(T) = M_s(0)\left[1 - s\left(\frac{T}{T_C}\right)^{3/2} - (1-s)\left(\frac{T}{T_C}\right)^{5/2}\right]^{1/3},$$

(1)

one obtains $T_C = (900 \pm 100)$ K for sample A and $T_C = (650 \pm 25)$ K for sample B. In Eq. (1), $M_s(0)$ denotes the saturation magnetization at $T = 0$ K, and s is a parameter related to the exchange constant and other properties. One can see that M_s and T_C in sample A are both larger than those in sample B. This is consistent with the previous observation that in free layers with nonmagnetic spacers higher M_s gives rise to higher T_C [17].

With the saturation induction, $4\pi M_s$, and effective anisotropy field, H_{eff}, data in Fig. 1, one can evaluate the interfacial anisotropy constant as $K_i = (1/2)M_s H_{\text{eff}} t_F + 2\pi M_s^2 t_F$. The K_i values at room temperature are given in Table I.

C. Room-temperature ferromagnetic resonance

Prior to high-temperature FMR measurements, room-temperature measurements were carried out on the samples with two distinct techniques: (1) cavity FMR and (2) vector network analyzer (VNA) FMR. The cavity FMR measurements were conducted with the high-temperature FMR system described in detail in Sec. II D. The measurements used six high-quality cylindrical cavities with resonance frequencies in the K_u band. The VNA FMR experiments
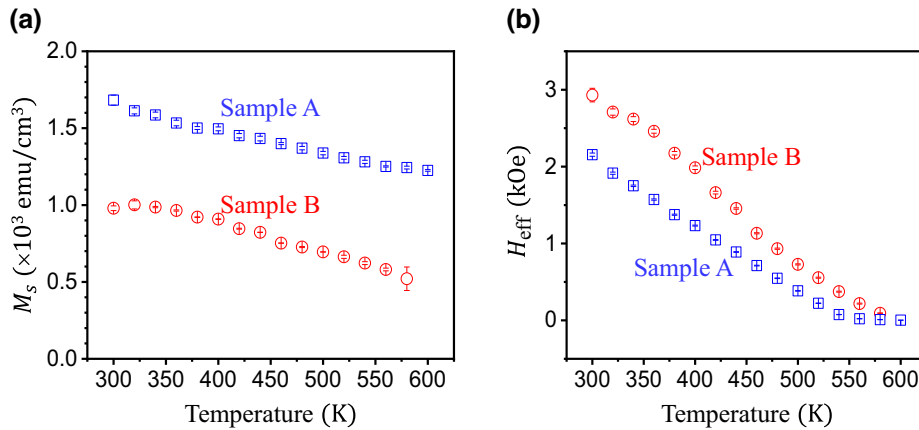

FIG. 1. Static magnetic properties of sample A and sample B. (a) Saturation magnetization, M_s, as a function of temperature (T). (b) Effective anisotropy field, $H_{\text{eff}} = H_u - 4\pi M_s$, as a function of T, where H_u and $4\pi M_s$ denote the perpendicular anisotropy field and saturation induction, respectively.

TABLE II. Comparison of room-temperature FMR results for both samples measured with two different techniques: (1) cavity FMR and (2) VNA FMR. For (1), the FMR measurements were carried out with six cylindrical cavities in the K_u band for which the frequency ranged from 12.4 to 18 GHz. For (2), the FMR measurements made use of a coplanar waveguide and a VNA over a frequency range from 13 to 42 GHz. All the measurements were performed under a perpendicular magnetic field.

Property	Sample A		Sample B	
	Cavity FMR	VNA FMR	Cavity FMR	VNA FMR
Effective anisotropy field, H_{eff} (Oe)	2150 ± 118	2235 ± 3	3099 ± 75 2970 ± 15	2990 ± 3 2984 ± 3
Damping constant, α ($\times 10^{-3}$)	3.5 ± 0.9	3.5 ± 0.2	8.7 ± 2.2 9.7 ± 0.5	11.4 ± 0.2 11.6 ± 0.3
Inhomogeneous line broadening, ΔH_0 (Oe)	133.1 ± 8.7	114 ± 4	104 ± 5 118 ± 22	73 ± 4 70.6 ± 5.5

involved the measurement of the scattering parameters of a coplanar waveguide and sample structure by a VNA system [18,19]. All the measurements were performed under a perpendicular magnetic field.

Table II presents representative room-temperature FMR data. The effective anisotropy field, H_{eff}, values were obtained by fitting the FMR field, H_{FMR}, versus microwave frequency, f, data to the Kittel equation:

$$2\pi f = |\gamma|(H_{\text{FMR}} + H_{\text{eff}}), \qquad (2)$$

where $|\gamma|$ is the absolute gyromagnetic ratio. The Gilbert damping constant, α, and the inhomogeneous line broadening, ΔH_0, were obtained by fitting the FMR linewidth, ΔH, versus f data to

$$\Delta H = \frac{1}{\sqrt{3}}\left[\frac{2\alpha}{|\gamma|}(2\pi f) + \Delta H_0\right]. \qquad (3)$$

Two remarks should be made about Eq. (3). First, the linewidth, ΔH, refers to the peak-to-peak linewidth, which is a factor of $\sqrt{3}$ smaller than the full width at half maximum linewidth. Second, ΔH_0 does not represent loss; it is the broadening of the FMR line due to the spatial inhomogeneity of the material properties across the sample, such as the spatial variation of M_s or H_u. For data in the fourth column of Table II, the second value in each cell was measured without the vacuum chamber and its associated components and with smaller field steps in comparison with the other values measured by the cavities. The data in the fifth column were obtained on the same samples through two separate measurements.

One can see three major results from Table II. First, the two sets of data measured by the two FMR techniques are fairly consistent with each other. Second, in contrast to the nearly perfect agreement between the two damping values for sample A, the damping values for sample B are slightly different. Possible reasons for this difference include that the FMR signals from sample B are weaker than those from sample A, which is due to the fact that sample B has smaller magnetization and larger damping

than sample A. Third, the parameters measured by the cavity technique have larger error bars than those measured by the VNA technique. This is because the cavity technique is limited by the number of microwave cavities available (six cavities) and their total frequency bandwidth (about 5.3 GHz), whereas the VNA FMR technique can measure almost continuously across a much wider frequency range (about 29 GHz). However, the VNA FMR technique is limited to room-temperature measurements. Note that for the room-temperature α values shown in Table I, the one for sample A is the same as the corresponding value in Table II measured by the cavity technique, while the one for sample B is the average of the two values in Table II measured by the cavity technique.

D. High-temperature ferromagnetic resonance

The high-temperature FMR measurements were carried out with a system that was an adaptation of a fixed-frequency cavity FMR setup [20–22]. Figure 2 shows a schematic diagram of the system. The major components include a diamond rod, a ceramic heater, a cylindrical cavity, and a vacuum chamber. The MRAM free-layer sample is adhered with an aluminum nitride adhesive (Aremco Ceramabond 865) to one end of a diamond rod, the other end of which is affixed to a ceramic heater, as illustrated in Fig. 2. The diamond rod loads the sample into the cavity through a small hole at the center of the bottom of the cavity. The microwave in the cavity is in the TE_{011} mode. The diamond rod is inserted along the central cylindrical axis of the cavity such that the sample is subject to an in-plane microwave magnetic field (**h**) and receives the maximum magnetic power and minimum electric power from the microwave. To minimize sample degradation and to avoid heat loss to surroundings, the cavity-diamond-heater assembly is housed in a chamber that has vacuum on the order of 10^{-5} torr. Although not shown in Fig. 2, an electromagnet applies a static magnetic field (**H**) to magnetize the sample along the film normal direction. Data presented below were measured with six K_u-band cylindrical cavities. The resonance frequencies of these cavities
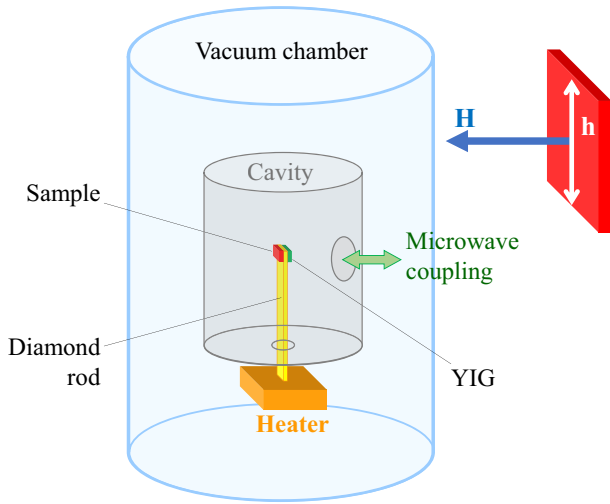
FIG. 2. Experimental setup for high-temperature ferromagnetic resonance. An MRAM free-layer sample is loaded to a cylindrical cavity via a diamond rod. The diamond rod also transfers heat from a ceramic heater outside the cavity to the sample. The sample is subject to a microwave magnetic field (**h**) that is along the cavity cylindrical axis (vertical) and an external static magnetic field (**H**) that is along the film normal direction (horizontal). An YIG thin film is affixed to the diamond rod on the opposite side of the MRAM free-layer sample. The YIG film is measured for temperature determination.

are 12.4, 13.2, 14.1, 15.3, 17.3, and 17.7 GHz; the corresponding unloaded quality factors are 13 100, 15 000, 6500, 9300, 6200, and 17 700, respectively.

For each measurement, the external magnetic field is swept, and the microwave power reflected from the cavity is recorded as a function of the field using a Schottky diode (Herotek DZ1026). The obtained power absorption versus field profile ideally has a Lorentzian shape. However, to increase the signal-to-noise ratio, the measurement uses field modulation and lock-in detection techniques, which means that what is measured is the derivative of the microwave power absorption versus field responses. In other words, each FMR profile measured has a shape of the derivative of a Lorentzian function.

Design considerations of the microwave cavities determine that the temperature of the sample cannot be measured directly. For example, the insertion of a conductive thermocouple into the cavity to measure the temperature would significantly reduce the quality factor of the cavity, and thus, the quality and strength of the FMR signals. The ceramic heater can be calibrated separately from the electric voltage applied to it, but the sample temperature is instead determined *in situ* by making a second FMR measurement on an yttrium iron garnet (YIG) thin-film element. The YIG film element is a square with a width of about 2 mm. The YIG film is 15.1 μm thick and grown on a single-crystal gadolinium gallium garnet (GGG) substrate by liquid-phase epitaxy. It is attached to the diamond

rod on the opposite side of the MRAM free-layer sample, with the film side facing the diamond rod. At equilibrium, the average temperatures of the free-layer sample and the YIG film should be approximately the same.

The YIG film has multiple advantages for use as a reference material for temperature determination. It is an insulator that has a low impact on the quality factor of the microwave cavity; it has a strong resonance that is easy to measure, even near T_C, and for a given microwave frequency, the resonant field of the YIG film is well separated from that of the free-layer sample. Additionally, the YIG film has negligible magnetic anisotropy, so one can directly correlate the FMR field versus temperature data with the saturation induction ($4\pi M_s$) versus temperature data obtained from the static magnetic measurements. This final point provides a method to effectively determine the sample temperature, as detailed below. One downside of the YIG film is its relatively low T_C, which limits this method to $T \approx 560$ K.

Figure 3 shows how the YIG measurements enable the determination of the sample temperature in the high-temperature FMR measurement. Graph (a) presents an FMR profile measured on the YIG film with the 17.7-GHz cavity at a high temperature, T, to be determined. Graph (b) presents the profile that is the integration of the one in graph (a). Graph (c) gives $4\pi M_s$ versus T data measured by a PPMS. All the measurements were carried out with a perpendicular magnetic field. The multiple resonances shown in graphs (a) and (b) correspond to the standing waves of the forward-volume magnetostatic waves across the lateral dimensions of the YIG film element. The strongest resonance at the high-field side is centered at a field close to the FMR field (H_{FMR}). Data in graph (c) are the $4\pi M_s$ values normalized to the value measured at room temperature. The data indicate $T_C \approx 560$ K, which is expected. The nonzero values at $T > 560$ K are associated with the magnetic moments in the paramagnetic GGG substrate.

Temperature determination involves the following major steps:

(1) Use the integrated FMR profile to determine H_{FMR}, as indicated in Fig. 3(b).
(2) Use the H_{FMR} value and the Kittel equation, Eq. (2), to estimate the $4\pi M_s$ value.
(3) Normalize the $4\pi M_s$ value from step (2) to the value measured at room temperature.
(4) Use the normalized value and the plot in Fig. 3(c) to determine the temperature, as indicated by the two arrows in Fig. 3(c).

III. HIGH-TEMPERATURE FERROMAGNETIC RESONANCE RESULTS

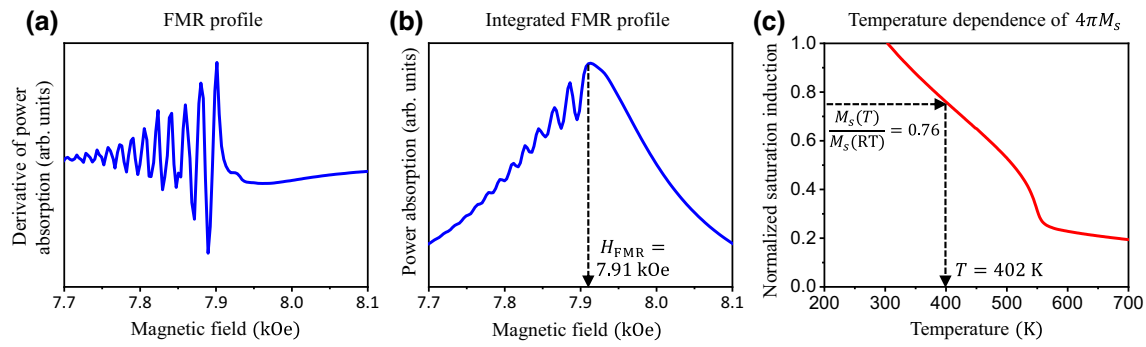The high-temperature FMR measurements made use of the six K_u-band cylindrical cavities described in Sec. II D.

FIG. 3.   Temperature determination through static and FMR measurements of an YIG thin film. (a) High-temperature FMR profile measured on an YIG film. (b) FMR profile after the integration of the profile in (a). (c) Saturation induction, $4\pi M_s$, of the YIG film measured as a function of temperature using a physical property measurement system. Values in (c) are normalized to the $4\pi M_s$ value measured at room temperature, namely, $4\pi M_s(\text{RT})$. Temperature determination involves the following major steps: (1) determine the FMR field (H_{FMR}), as indicated by the vertical arrow in (b); (2) use H_{FMR} and the Kittel equation to determined $4\pi M_s$; and (3) use the $4\pi M_s$ value, indicated by the horizonal arrow in (c), and the $4\pi M_s$ against temperature plot to determine the temperature, indicated by the vertical arrow in (c).

For each cavity, a sequence of measurements were conducted at different temperatures (T) that increased from 300 to 520 K. When switching to a different cavity, a new piece of the free-layer sample was used. The upper temperature limit is determined by the quality of the FMR signals, which tend to weaken and distort as the sample temperature approaches T_c.

Figure 4 presents representative FMR profiles measured on sample A, the low-α free-layer sample. Data in each row were measured with one and the same microwave cavity, with the cavity resonance frequency indicated on the left side. Data in each column were measured at the same temperature, as indicated at the top of each column. In each graph, the blue dots represent the derivative of the
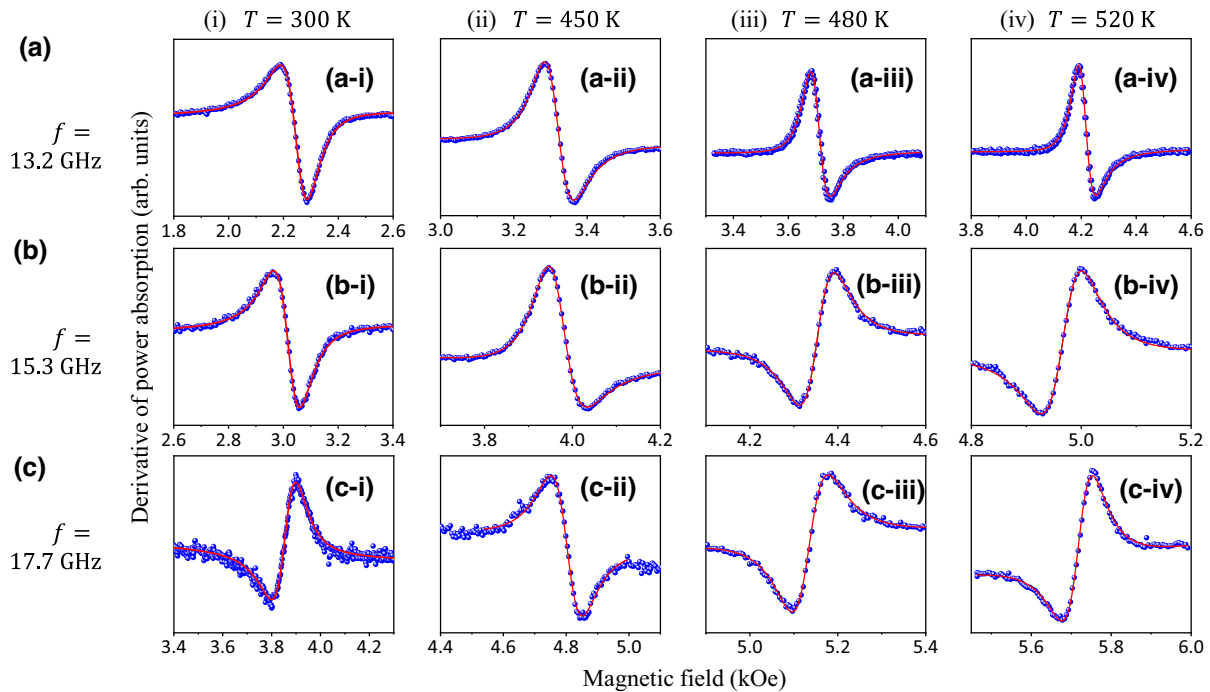

FIG. 4.   Representative FMR profiles measured on sample A. Data in each row were measured with one and the same cavity, with the cavity frequency given on the left side. Data in each column were measured at the same temperature, as indicated at the top. Blue dots show the experimental data points, while the red curves are numerical fits.

microwave power absorption measured as a function of the magnetic field (H), while the red curve is a fit to the derivative of a Lorentzian trial function. The fitting yields the FMR field (H_{FMR}) and peak-to-peak linewidth (ΔH) values, which are presented in Fig. 6.

Three results are evident from the FMR data in Fig. 4. First, with an increase in temperature, the resonance shifts to a higher magnetic field. This is consistent with the fact that the effectively anisotropy field, H_{eff}, decreases with temperature, as shown in Fig. 1(b), and to maintain the FMR at the same frequency a higher field is needed, according to Eq. (2). Second, with an increase in the cavity frequency, the resonance also shifts to a higher field. This is a reflection of the linear scaling of the FMR frequency with the magnetic field, as shown in Eq. (2). Third, some of the FMR profiles, such as those in Figs. 4(a-i) and 4(b-ii), do not show the usual antisymmetric responses. These profile distortions are likely due to the mixing of the real and imaginary parts of the complex magnetic susceptibility (χ), as discussed in Refs. [23,24]. For those FMR profiles, the numerical fitting used an equation that had two components: (1) a usual antisymmetric component associated with the imaginary part of χ, and (2) a symmetric component associated with the real part of χ.

Figure 5 presents representative FMR profiles measured on sample B, the conventional free-layer sample. Data are presented in the same format as those in Fig. 4. One observes the same results as those described above for

Fig. 4. There are also quantitative differences in the FMR properties of the two samples, which are discussed shortly. One difference of particular note here is as follows: the derivative lineshape for sample B begins to weaken and become steplike, even at $T = 450$ K, whereas sample A maintains a clear derivative lineshape over the entire temperature range. One can attribute this difference to the differences in the Curie temperatures and damping constants of the two samples. As shown in Table I, sample B has a much lower T_C than sample A. As the sample temperature approaches T_C, the magnetic moment becomes small and the measured resonance strength becomes weak. Sample B also has a larger Gilbert damping constant (α) for all the temperatures, as detailed below, which also contributes to weaker FMR signals.

Turn now to the H_{FMR} and ΔH results obtained from the numerical fitting of the experimental FMR profiles described above. Figure 6 presents the results for sample A. The first row gives H_{FMR} data measured at three different temperatures, as indicated. In each graph, the blue dots show the H_{FMR} values at different frequencies, while the red lines are numerical fits to Eq. (2). The fitting-yielded effective anisotropy fields (H_{eff}) and the absolute gyromagnetic ratios ($|\gamma|$) are indicated. The second row gives ΔH data that correspond to the H_{FMR} data in the first row. In each graph, the blue dots show the ΔH values at different frequencies, while the red lines are fits to Eq. (3). The fitting-yielded Gilbert damping constant
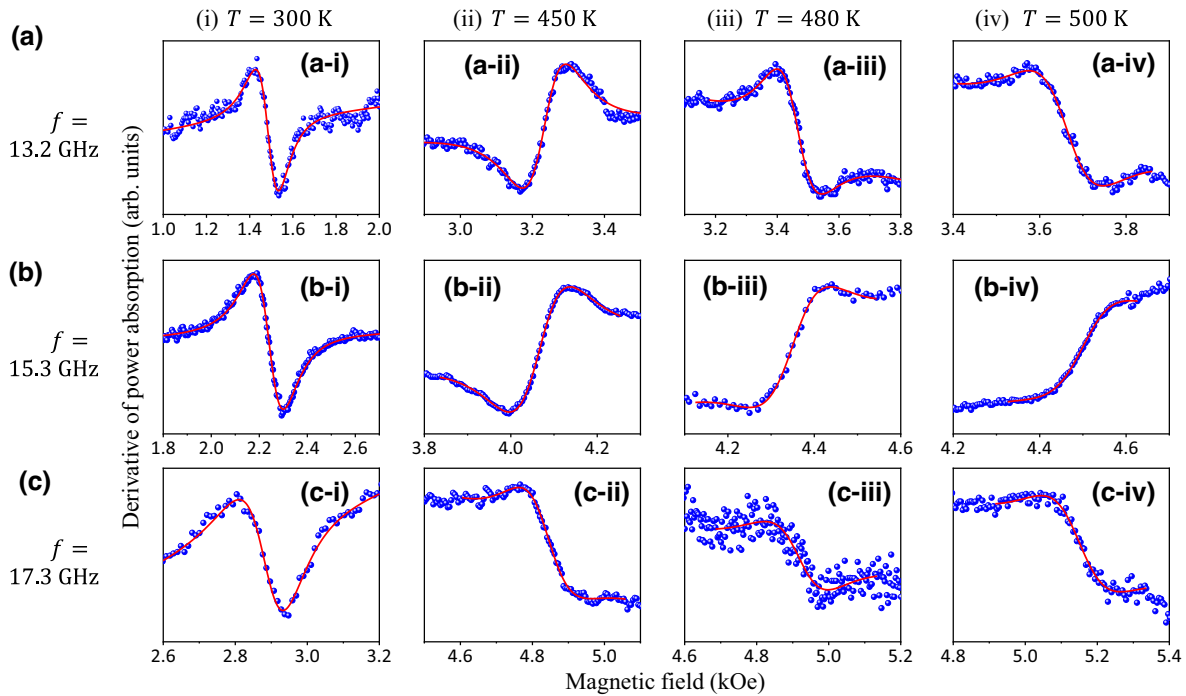

FIG. 5. Representative FMR profiles measured on sample B. Data in each row were measured with one and the same cavity, with the cavity frequency given on the left side. Data in each column were measured at the same temperature, as indicated at the top. Blue dots show the experimental data points, while the red curves are numerical fits.

(α) and inhomogeneous line broadening (ΔH_0) values are indicated in the graphs. Two notes should be made about data in Fig. 6. First, the multiple data points for a given cavity and a given temperature resulted from repeated measurements. Second, only data from three cavities are presented. This is because the 12.4-GHz cavity had not been fabricated at the time of the measurement of sample A, and the relatively low quality factors of the 14.1- and 17.3-GHz cavities led to poor FMR signals.

Data in Fig. 6 show important results on how H_{eff}, α, and ΔH_0 vary with temperature, as discussed shortly. Presented here are a few remarks about the numerical fitting in Fig. 6. First, data in the first row can be nicely fit. This indicates that the sample temperatures in the three different cavities are equivalent to each other. One can also notice that, in comparison with those in Figs. 6(a-i) and 6(a-ii), the data points in Fig. 6(a-iii) are slightly more scattered, even though the trend is still well defined. This means that at relatively high temperatures the repeated points have more variance at each frequency. Possible reasons for this include that (1) the accuracy of the temperature determination described in Sec. II D is reduced as the temperature approaches the Curie temperature of the YIG film, and (2) at high temperature the FMR signals of the free-layer samples generally tend to become weaker due to the reduced magnetic moments, as shown in Fig. 1(a), and the

enhanced damping, as shown in Fig. 8(a). Second, in contrast to data in the first row, the linewidth data in the second row are more scattered, which indicates that the variance in linewidth measurements is more pronounced. Nevertheless, the linewidth data clearly show linearly increasing trends with frequency, as expected according to Eq. (3). The fitting of data to Eq. (3) yields α and ΔH_0 values with relatively large uncertainties that are the reflections of the scattering of the data points.

Figure 7 presents H_{FMR} and ΔH data and the corresponding fits for sample B, using the same format as that in Fig. 6. The fitting-yielded results for H_{eff}, α, and ΔH_0 are discussed shortly. Three remarks about these data are as follows. First, the ΔH versus cavity-frequency (f) data in the second row are more scattered than the H_{FMR} versus f data in the first row, similar to data presented in Fig. 6. Second, the fitting shown in Fig. 7(b-i) seems to be done with the 17.7-GHz data point excluded, but, in fact, it does include that data point. The fact that the fitting line strongly favors the low-frequency data points is because the uncertainties of the low-frequency points are smaller than the 17.7-GHz data point. This is also true for the fitting in Fig. 6(b-i). Third, in Fig. 7(b-ii) there are three data points for 17.3 GHz. The point with the relatively small uncertainty was measured first, while the other two with large uncertainties were collected in the repeated measurements
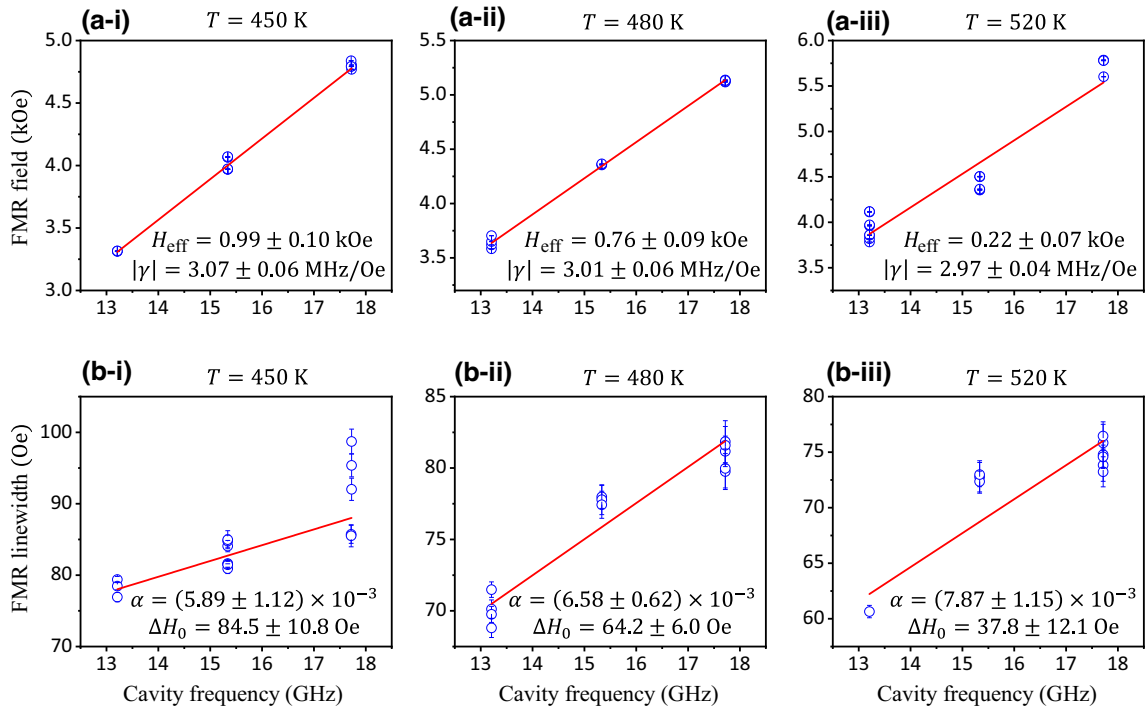

FIG. 6. FMR properties of sample A at three different temperatures, as indicated. Graphs in the first row show the FMR fields (H_{FMR}) at different cavity frequencies (f). Blue dots show the experimental data, while the red lines are numerical fits to Eq. (2). Graphs in the second row show the FMR linewidths (ΔH) at different cavity frequencies. Blue dots show the data and the red lines are fits to Eq. (3).

FIG. 7.   FMR properties of sample B at three different temperatures, as indicated. Graphs in the first row show the FMR fields (H_{FMR}) at different cavity frequencies (f). Blue dots show the experimental data, while the red lines are numerical fits to Eq. (2). Graphs in the second row show the FMR linewidths (ΔH) at different cavity frequencies. Blue dots show the data and the red lines are fits to Eq. (3).
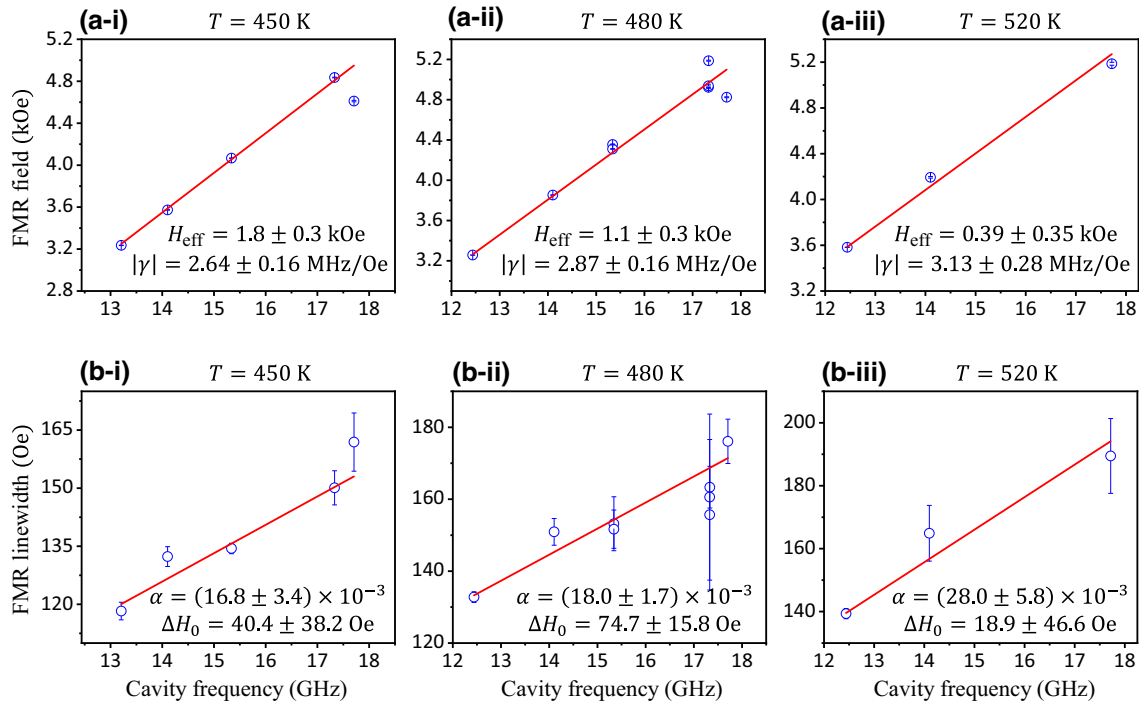
for which the FMR signals were weaker. However, if the two points with large uncertainties were excluded during the fitting process, the resulting fit would not have notable changes.

It should be mentioned that the absolute gyromagnetic ratios in Figs. 6 and 7 range from 2.64 to 3.13 MHz/Oe. This range appears to be unreasonably wide, but this does not pose a problem because the uncertainties of those $|\gamma|$ values are high. The large uncertainties result mostly from the limited number of frequency points.

Consider now the H_{eff}, α, and ΔH_0 results obtained from the numerical fittings, such as those shown by the red lines in Figs. 6 and 7. Figure 8 presents the results. Graphs (a), (b), and (c) show α, H_{eff}, and ΔH_0, respectively, as a function of the sample temperature (T). In each graph, the blue and red symbols show the results for sample A and sample B, respectively. The values at $T = 300$ K are the same as those presented in Tables I and II. The values at $T = 520$ K are also listed in Table I. The two arrows in graph (a) are drawn as guides for the eye to show the overall trends.

The damping values in Fig. 8(a) show three key conclusions of this work: (1) over the entire temperature range, the damping constant, α, of sample A is smaller than that of sample B; (2) α increases with the temperature in both samples; and (3) the increase of α is relatively moderate in sample A but is more pronounced and seems to be exponential in sample B. The first conclusion explains why the

switching current in the STT MRAM device made of the low-α free layer is lower than that in the device made of the conventional free layer [8]. As pointed out in Sec. I, the critical current for switching scales linearly with the damping constant of the free layer; the smaller the damping is, the lower the switching current is. The first and third conclusions together clearly establish the technological advantage of sample A over sample B from the perspective of the STT MRAM application. The third conclusion is technologically important, because the operation of STT MRAM cells usually occurs above room temperature, as noted earlier.

To understand the physics underlying the three conclusions listed above, turn now to a discussion on the possible damping processes in the free-layer samples in this work. Generally speaking, a ferromagnetic thin film can host the following six damping processes: (1) magnon-phonon scattering, (2) eddy-current-associated damping, (3) magnon-electron scattering associated with Fermi-surface breathing, (4) spin-flip magnon-electron scattering (SF MES), (5) two-magnon scattering, and (6) spin pumping. Processes (1)–(4) are intrinsic, while processes (5) and (6) are extrinsic.

Magnon-phonon scattering occurs in all magnetic materials, but its contribution to the overall damping in a metallic thin film is usually much smaller than the contributions from the magnon-electron scattering processes
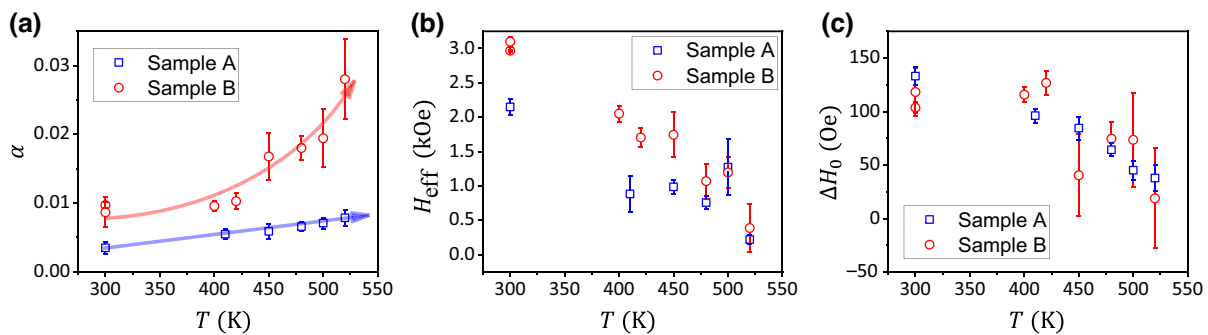
FIG. 8. High-temperature FMR results of sample A and sample B. Graphs (a)–(c) show the Gilbert damping constant, α; the effective anisotropy field, H_{eff}; and the inhomogeneous line broadening, ΔH_0, respectively, as a function of sample temperature T. Two arrows in graph (a) serve as guides for the eye to show the overall trends.

[25]. The eddy-current-associated damping is nontrivial in relatively thick films [26]. For the free layers in this work, the thicknesses are substantially smaller than skin depth, and eddy-current-produced damping can therefore be neglected. The third damping process on the list is the Fermi-surface-breathing-associated magnon-electron scattering, which is often referred to as the intraband scattering [9–12]. The damping associated with this scattering increases with a decrease in temperature. As a result, it is usually smaller than the damping produced by the SF MES above room temperature. The fourth one on the list is the SF-MES process, which is often referred to as interband scattering [9–12]. This process involves both momentum and energy conservation, which can be more easily satisfied at higher temperatures. As such, damping due to the SF-MES process usually increases with an increase in temperature.

The two-magnon scattering, the fifth one on the list, involves the scattering of a uniform magnon to a nonuniform magnon by material imperfection; such imperfection includes grain misalignment, grain boundaries, line cracks, pores, and surface or interface roughness in the films [27–31]. This process, however, is absent in the free-layer samples in this work because the FMR experiments make use of perpendicular magnetic fields, as illustrated in Fig. 2. In thin films magnetized perpendicularly, there are no degenerate spin-wave modes at the FMR frequency available for two-magnon scattering.

The spin-pumping process, the last one on the above list, involves the pumping of a pure spin current by the precessing moments in a magnetic thin film into a neighboring nonmagnetic metallic film. This process gives rise to a damping enhancement in the magnetic film, and such an enhancement can be substantial if the nonmagnetic film is made of a material with strong spin-orbit coupling, such as a heavy metal, a topological insulator, or a topological semimetal [32–36]. The W layers in the samples in this work are a heavy metal, but their thicknesses are substantially smaller than the spin-diffusion length. The nominal

thicknesses of the W layers in sample A and sample B are 0.2 and 3 Å, respectively, while the spin-diffusion length in W ranges from 21 to 35 Å [37]. For this reason, the damping contribution due to spin pumping into the W layers is expected to be weak. Nevertheless, the W layers may produce some damping through enhanced spin-flip scattering at the interfaces; previous work has shown damping enhancement in Co-Fe-B thin films due to neighboring ultrathin Ta films [38].

The above discussion indicates that, above room temperature, damping in the free layers in this work originates mainly from the SF-MES process, while the contributions from the other five mechanisms are either zero or relatively small. As mentioned earlier, the SF-MES process involves energy and momentum conservation, while the latter is easier to satisfy at high temperature. For this reason, the SF-MES-produced damping increases with an increase in temperature. This explains why α increases with T in Fig. 8(a). The damping increase becomes more pronounced when the temperature is closer to T_c [11]. This justifies the larger increase in α for sample B than that for sample A. The T_c values for sample A and sample B are about 900 and 650 K, respectively, so, in comparison with sample A, the temperature of sample B is closer to T_c. It is for the same reason that α in sample B is larger than that in sample A, as shown in Fig. 8(a). The other minor reason for this difference is that in sample B there might be a small damping due to spin pumping from the magnetic layers to the W layer, while in sample A such damping is much smaller because the nominal thickness of the W layer (0.2 Å) is too small to form a continuous monolayer of W.

We turn now to the results presented in Figs. 8(b) and 8(c). Though being scattered slightly, the data points in Fig. 8(b) clearly show overall decreasing trends. As the sample temperature increases from 300 to 520 K, the effective anisotropy field, H_{eff}, decreases from about 2.15 kOe to about 0.22 kOe in sample A and decreases from about 3.04 kOe to about 0.39 kOe in sample B. These values are consistent with those shown in Fig. 1(b),

and this agreement provides strong justification for the high-temperature FMR data. The data in Fig. 8(c) show that, in both samples, the inhomogeneous line broadening, ΔH_0, decreases with an increase in temperature. Since the decrease of the saturation magnetization, M_s, over the same temperature range is relatively moderate, as shown in Fig. 1(a), the data in Fig. 8(c) indicate that ΔH_0 originates mostly from the spatial inhomogeneity of the anisotropy in the samples, not the inhomogeneity of magnetization.

IV. CONCLUSIONS

With a microwave-cavity-based FMR system, high-temperature frequency-dependent FMR measurements have been carried out on two free-layer samples: a low-α free layer with split W layers and a conventional free layer with a single W layer. The measurements and analyses have yielded the following results for the high-temperature damping properties: (1) the damping constant of the low-α free layer is smaller than that of the conventional free layer over the entire temperature range from 300 to 520 K; (2) the damping constant increases monotonically with temperature in both the low-α and conventional free layers; and (3) this damping increase is relatively modest and almost linear in the low-α free layer but is more pronounced and nearly exponential in the conventional free layer. These results clearly explain the experimental observation of smaller switching current in the STT MRAM device made of the low-α free layer than in that made of the conventional free layer [8]. They evidently establish the advantages and merits of the low-α free layer over the conventional free layer for the STT MRAM application.

The above-summarized results on damping can be interpreted in terms of the SF MES [9–12] and the difference of the Curie temperatures of the two free layers [8]. The SF-MES process involves both momentum and energy conservation. Since such conservation is easier to satisfy at higher temperatures, the process becomes stronger and produces larger damping as the temperature is increased towards the Curie temperature. This is why the damping constants in both free layers increase monotonically as the temperature increases from 300 to 520 K. On the other hand, the Curie temperature in the conventional free layer is much lower than that in the low-α free layer. As such, 520 K, the highest temperature in the FMR experiments, is closer to the Curie temperature in the conventional free layer than in the low-α free layer, and the damping increase in the conventional free layer is therefore more pronounced. This explains why the damping constant in the conventional free layer increases more rapidly and is also larger than in the low-α free layer.

In addition to the above damping results, the high-temperature FMR measurements have also yielded important information about the temperature dependence of the effective perpendicular anisotropy fields and inhomogeneous line broadening. The effective magnetic fields in the two free layers vary with temperature in the same quantitative manner as that found from the static magnetic measurements. This consistency provides clear justification for the high-temperature FMR data. As the temperature increases from 300 to 520 K, the inhomogeneous line broadening decreases substantially in both free layers. This indicates that line broadening originates mainly from the spatial inhomogeneity of the perpendicular anisotropy in the samples, because magnetization decreases over the same temperature range are modest, according to static magnetic measurements.

[1] K. C. Chun, H. Zhao, J. D. Harms, T. Kim, J. Wang, and C. H. Kim, A scaling roadmap and performance evaluation of in-plane and perpendicular MTJ based STT-MRAMs for high-density cache memory, IEEE J. Solid-State Circuits **48**, 598 (2013).

[2] B. Tudu and A. Tiwari, Recent developments in perpendicular magnetic anisotropy thin films for data storage applications, Vacuum **146**, 329 (2017).

[3] R. Sbiaa, H. Meng, and S. N. Piramanayagam, Materials with perpendicular magnetic anisotropy for magnetic random access memory, Phys. Status Solidi RRL **5**, 413 (2011).

[4] A. V. Khvalkovskiy, D. Apalkov, S. Watts, R. Chepulskii, R. S. Beach, A. Ong, X. Tang, A. Driskill-Smith, W. H. Butler, and P. B. Visscher, Basic principles of STT-MRAM cell operation in memory arrays, J. Phys. D: Appl. Phys. **46**, 074001 (2013).

[5] H. Sato, M. Yamanouchi, S. Ikeda, S. Fukami, F. Matsukura, and H. Ohno, Perpendicular-anisotropy CoFeB-MgO magnetic tunnel junctions with a MgO/CoFeB/Ta/CoFeB/MgO recording structure, Appl. Phys. Lett. **101**, 022414 (2012).

[6] S. Couet, T. Devolder, J. Swerts, S. Mertens, T. Lin, E. Liu, S. Van Elshocht, and G. Sankar Kar, Impact of Ta and W-based spacers in double MgO STT-MRAM free layers on perpendicular anisotropy and damping, Appl. Phys. Lett. **111**, 152406 (2017).

[7] J. Chatterjee, A. Chavent, F. Fettar, S. Auffret, C. Ducruet, I. Joumard, L. Vila, R. C. Sousa, L. Prejbeanu, and B. Dieny, Reduced Thermal Variation of Perpendicular Magnetic Anisotropy in Magnetically Stiffened Dual-W Composite Storage Layer for Spin-Transfer-Torque Magnetic Random-Access Memory, Phys. Rev. Appl. **12**, 044043 (2019).

[8] T. S. Santos, G. Mihajlović, N. Smith, J. Li, M. Carey, J. A. Katine, and B. D. Terris, Ultrathin perpendicular free layers

for lowering the switching current in STT-MRAM, J. Appl. Phys. **128,** 113904 (2020).

[9] J. Kuneš and V. Kamberský, First-principles investigation of the damping of fast magnetization precession in ferromagnetic 3*d* metals, Phys. Rev. B **65,** 212411 (2002).

[10] V. Kamberský, Spin-orbital Gilbert damping in common magnetic materials, Phys. Rev. B **76,** 134416 (2007).

[11] K. Gilmore, Y. U. Idzerda, and M. D. Stiles, Identification of the Dominant Precession-Damping Mechanism in Fe, Co, and Ni by First-Principles Calculations, Phys. Rev. Lett. **99,** 027204 (2007).

[12] T. Qu and R. H. Victora, Effect of substitutional defects on Kambersky damping in L10 magnetic materials, Appl. Phys. Lett. **106,** 072404 (2015).

[13] J. Swerts, S. Mertens, T. Lin, S. Couet, Y. Tomczak, K. Sankaran, G. Pourtois, W. Kim, J. Meersschaut, L. Souriau, D. Radisic, S. Van Elshocht, G. Kar, and A. Furnemont, BEOL compatible high tunnel magneto resistance perpendicular magnetic tunnel junctions using a sacrificial Mg layer as CoFeB free layer cap, Appl. Phys. Lett. **106,** 262407 (2015).

[14] M. D. Kuz'min, Shape of Temperature Dependence of Spontaneous Magnetization of Ferromagnets: Quantitative Analysis, Phys. Rev. Lett. **94,** 107204 (2005).

[15] M. D. Kuz'min, M. Richter, and A. N. Yaresko, Factors determining the shape of the temperature dependence of the spontaneous magnetization of a ferromagnet, Phys. Rev. B **73,** 100401 (2006).

[16] S. Srivastava, A. P. Chen, T. Dutta, R. Ramaswamy, J. Son, M. S. M. Saifullah, K. Yamane, K. Lee, K. Teo, Y. P. Feng, and H. Yang, Effect of $(Co_xFe_{1-x})_{80}B_{20}$ Composition of the Magnetic Properties of the Free Layer in Double-Barrier Magnetic Tunnel Junctions, Phys. Rev. Appl. **10,** 024031 (2018).

[17] J. M. Iwata-Harms, G. Jan, H. Liu, S. Serrano-Guisan, J. Zhu, L. Thomas, R. Tong, V. Sundar, and P. Wang, High-temperature thermal stability driven by magnetization dilution in CoFeB free layers for spin-transfer-torque magnetic random access memory, Sci. Rep. **8,** 14409 (2018).

[18] J. Ding, C. Liu, Y. Zhang, U. Erugu, Z. Quan, R. Yu, E. McCollum, S. Mo, S. Yang, H. Ding, X. Xu, J. Tang, X. Yang, and M. Wu, Nanometer-Thick Yttrium Iron Garnet Films with Perpendicular Anisotropy and Low Damping, Phys. Rev. Appl. **14,** 014017 (2020).

[19] D. Richardson, K. Srinivasan, S. Katz, and M. Wu, Quantification of intergranular exchange coupling in CoPtCr-based perpendicular recording media via ferromagnetic resonance measurements, Appl. Phys. Lett. **111,** 183506 (2017).

[20] D. Richardson, S. Katz, J. Wang, Y. K. Takahashi, K. Srinivasan, A. Kalitsov, K. Hono, A. Ajan, and M. Wu, Near-T_c Ferromagnetic Resonance and Damping in FePt-Based Heat-Assisted Magnetic Recording Media, Phys. Rev. Appl. **10,** 054046 (2018).

[21] D. Richarson, K. Srinivasan, A. Kalitsov, A. Ajan, S. Jain, S. Katz, and M. Wu, Interlayer Exchange Coupling in Magnetic Hard-Soft Bilayered Structures, Phys. Rev. Appl. **11,** 044016 (2019).

[22] C. Liu, K. Srinivasan, A. Ajan, E. McCollum, A. Kalitsov, V. Kalappattil, and M. Wu, Ferromagnetic resonance in

FePt thin films at elevated temperatures, J. Magn. Magn. Mater. **563,** 169988 (2022).

[23] E. Montoya, T. McKinnon, A. Zamani, E. Girt, and B. Heinrich, Broadband ferromagnetic resonance system and methods for ultrathin magnetic films, J. Magn. Magn. Mater. **356,** 12 (2014).

[24] G. Woltersdorf, PhD thesis, Simon Fraser University, 2004.

[25] M. Sparks, *Ferromagnetic-Relaxation Theory* (McGraw-Hill, New York, 1964).

[26] C. Scheck, L. Cheng, and W. E. Bailey, Low damping in epitaxial sputtered iron films, Appl. Phys. Lett. **88,** 252510 (2006).

[27] R. D. McMichael and P. Krivosik, Classical model of extrinsic ferromagnetic resonance linewidth in ultrathin films, IEEE Trans. Magn. **40,** 2 (2004).

[28] P. Krivosik, N. Mo, S. Kalarickal, and C. E. Patton, Hamiltonian formalism for two magnon scattering microwave relaxation: Theory and applications, J. Appl. Phys. **101,** 083901 (2007).

[29] P. Landeros, R. E. Arias, and D. L. Mills, Two magnon scattering in ultrathin ferromagnets: The case where the magnetization is out of plane, Phys. Rev. B **77,** 214405 (2018).

[30] N. Mo, J. Hohlfeld, M. ul Islam, C. S. Brown, E. Girt, P. Krivosik, W. Tong, A. Rebei, and C. E. Patton, Origins of the damping in perpendicular media: Three component ferromagnetic resonance linewidth in Co-Cr-Pt alloy films, Appl. Phys. Lett. **92,** 022506 (2008).

[31] P. Krivosik, S. S. Kalarickal, N. Mo, S. Wu, and C. E. Patton, Ferromagnetic resonance and damping in granular Co−Cr films with perpendicular anisotropy, Appl. Phys. Lett. **95,** 052509 (2009).

[32] B. Heinrich and J. A. C. Bland, *Ultrathin Magnetic Structures: Fundamentals of Nanomagnetism* (Springer, Berlin, 2005).

[33] R. Urban, G. Woltersdorf, and B. Heinrich, Gilbert Damping in Single and Multilayer Ultrathin Films: Role of Interfaces in Nonlocal Spin Dynamics, Phys. Rev. Lett. **87,** 217204 (2001).

[34] Y. Tserkovnyak, A. Brataas, and G. E. W. Bauer, Enhanced Gilbert Damping in Thin Ferromagnetic Films, Phys. Rev. Lett. **88,** 117601 (2002).

[35] B. Heinrich, C. Burrowes, E. Montoya, B. Kardasz, E. Girt, Y. Song, Y. Sun, and M. Wu, Spin Pumping at the Magnetic Insulator (YIG)/Normal Metal (Au) Interfaces, Phys. Rev. Lett. **107,** 066604 (2011).

[36] J. Ding, C. Liu, Y. Zhang, V. Kalappattil, R. Yu, U. Erugu, J. Tang, H. Ding, H. Chen, and M. Wu, Large damping enhancement in Dirac-semimetal−ferromagnetic-metal layered structures caused by topological surface states, Adv. Funct. Mater. **31,** 2008411 (2021).

[37] D. JhaJhria, N. Behera, D. K. Pandya, and S. Chaudhary, Dependence of spin pumping in W/CoFeB heterostructures on the structural phase of tungsten, Phys. Rev. B **99,** 014430 (2019).

[38] S. Ikeda, K. Miura, H. Yamamoto, K. Mizunuma, H. D. Gan, M. Endo, S. Kanai, J. Hayakawa, F. Matsukura, and H. Ohno, A perpendicular-anisotropy CoFeB-MgO magnetic tunnel junction, Nat. Mater. **9,** 721 (2010).